Cerium oxides and cerium-platinum surface alloys on Pt(111) single-crystal surfaces studied by scanning tunneling microscopy

Ulrich Berner and Klaus-Dieter Schierbaum*
Abteilung für Materialwissenschaft, Institut für Physik der Kondensierten Materie, Heinrich-Heine-Universität Düsseldorf Universitätsstrasse 1, 40225 Düsseldorf, Germany

(Received 9 October 2001; revised manuscript received 21 December 2001; published 24 May 2002)

Three-dimensional clusters of metallic Ce are deposited on Pt(111) surfaces by thermal evaporation in ultrahigh vacuum. Different reactions occur upon heating of the sample in ultrahigh vacuum and during the exposure of oxygen that lead to distinct well-ordered surface phases. Their geometric structures are determined by scanning tunneling microscopy (STM). A two-dimensional ordered surface alloy of Pt_5Ce is obtained by annealing at 1000 K. It forms two different incommensurate overlayers on Pt(111) with long-distance spacings in the moiré patterns (13.7 and 14.8 Å). Hexagonally shaped two-dimensional islands are formed upon heating the Pt(111) single crystal with a submonolayer coverage of Ce at 900 K. They are localized at step edges. STM reveals a local 2×2 structure with respect to Pt(111). It is assigned to a precursor state of alloy formation. Ordered CeO_2 phases result from annealing the alloy at 1000 K in oxygen. The surface structure is consistent with oxygen-terminated fluorite-type $CeO_2(111)$. During decomposition of CeO_2 at 900 K, an oxide structure is identified which is attributed to an ultrathin ordered phase of surface-Ce_2O_3.

DOI: 10.1103/PhysRevB.65.235404 PACS number(s): 68.37.Ef, 68.47.De, 68.47.Gh

I. INTRODUCTION

Epitaxial metal oxide films grown on metal substrates in ultrahigh vacuum have been extensively studied for many years. A variety of investigations was motivated by the fact that such systems may provide well-defined surfaces of metal oxides, e.g., in cases where the corresponding single crystals are hard to cleave *in situ* or exhibit an unsufficient electrical conductivity to apply electron spectroscopic techniques. Well characterized ''model'' systems such as $\alpha-Cr_2O_3(0001)$ on Cr(110) (Ref. 1) and $Al_2O_3(0001)$ on NiAl(110) (Ref. 2) have been the subject of numerous investigations employing the huge variety of surface science tools.[3] A number of oxides, however, cannot be grown epitaxially from the base metal or its alloys due to the lattice mismatch or the large spatial change of the oxygen activity perpendicular to the interface. For such systems, low-index surfaces of noble metals such as Pt, Au, Pd, Rh, and Ru may serve as perfect substrates to deposit oxides by reactive evaporation of the metal in the presence of O_2 or by cycles of metal evaporation and oxidation. Specifically, thin magnetite $Fe_3O_4(111)$ films have been prepared on Pt(111),[4] V_2O_3 on Au(111),[5] and Pd(111),[6] and CeO_2 on Ru(0001) and Ni(111).[7] Scanning tunneling microscopy (STM) has shown that these ultrathin epitaxial oxide films may exhibit complicated surfaces including the coexistence of mesoscopic domains of different terminations and structures. Particularly, this is found for metals that can form oxides in several distinct oxidation states. The coexistence of islands of α-$Fe_2O_3(0001)$ and FeO(111) on Pt(111) surfaces and their arrangement to form superlattices have been termed biphase ordering.[8] For $\alpha-Fe_2O_3(0001)$ films on Pt(111), domains with Fe and the unexpected O termination have been observed, too.[9] For $Fe_3O_4(111)$ films on Pt(111) ordered biphases of Fe_3O_4 and FeO(111) have been found with STM, depending critically on parameters of the deposition process. An example for which oxide films reveal novel structures that are very different from their bulk counterparts is vanadium oxide on Pd(111). Surnev *et al.* have recently demonstrated that very thin layers of vanadium oxide exhibit coexisting surface phases [hexagonal $V_2O_3(2\times2)$, hexagonal VO_2, and rectangular VO_2] which are not stable as bulk structures.[10] These interfacial oxide layers transform into the stable bulklike V_2O_3 phase if a critical thickness of three monolayers is exceeded during film growth. The authors also expect such an effect for other oxides.

Heteroepitaxy is reported for ultrathin ceria films grown on Pt(111) surfaces.[11,12] In contrast to iron and vanadium oxides, CeO_2 is obtained here by oxidation of an ordered surface alloy phase between Ce and Pt. Such samples can be prepared by heating amorphous ceria overlayers on Pt(111) in ultrahigh vacuum at 1000 K as the result of decomposition of CeO_2 and intermixing of Ce and Pt. The Ce-Pt system shows complete miscibility within the entire composition range. The surface indicates a $(2\times2)+(2\times2)R30°$ superstructure in low-energy electron diffraction (LEED). Surface alloy formation on the topmost atomic plane is a well-known phenomenon which is reported for a variety of bulk miscible metal-on-metal systems such as, e.g., Pd-Cu but is also observed if the overlayer and the substrate exhibit bulk inmiscibility such as Au-Ni.[13] For platinum, a few overlayer systems has been reported that form ordered surface alloys such as Cr (Ref. 14) and Ag.[15] Previous LEED and STM studies have demonstrated that Ce overlayers on Pt(111) substrates yield a two-dimensional Pt_5Ce surface phase upon heating in u.h.v.[16] Similar to LEED results given in an ealier study,[11] a $(2\times2)+(2\times2)R30°$ LEED superstructure is found if a four monolayer Ce film on Pt(111) is annealed at 1000 K.

Reflection-adsorption infrared spectroscopy (RAIRS) and adsorption experiments with NO_2 give evidence that ordered surface phases of CeO_2 obtained through the oxidation of surface Pt_5Ce on Pt(111) are shaped similar to islands that do

not coalesce, even though these crystalline islands indicate a high-order commensurable growth with respect to the nonreconstructed Pt(111) surface.[17] The epitaxy gives rise to a well-orderd (1.4×1.4) superstructure in LEED. X-ray photoemission spectroscopy (XPS) of the Ce $3d$ core levels and valence band photoemission spectroscopy of the Ce $4f$ band gap state indicate a large deviation from ideal stoichiometry ($x\approx0.2$) of such thin granular ceria films (that have a nominal thickness of a few Å) after annealing in oxygen (6×10^{-5} mbar, 1000 K) . This value is remarkably larger when compared with polycrystalline thick films of CeO_2 ($\geqslant10$ nm) on recrystallized Pt foils after annealing in oxygen (10^{-4} mbar, 973 K, $x\leqslant0.02$).[18] Similar to the V_2O_3/Pt(111) system, this behavior was associated with the reducing property of the underlying metal substrate.

The decomposition of CeO_2/Pt(111) occurs upon heating the samples in u.h.v. and leads to ordered surface alloys which can be reoxidized again to a 1.4×1.4 oxide surface phase.[11,16] The transition between the ordered surface alloy and the ordered oxidic phase exhibits complete reversibility with respect to the chemical composition (as determined with XPS) and the long-range order (as determined with LEED) and is thermodynamically driven. Kinetic effects may, however, play a significant role so far details of the morphology and defect structure of the ceria phases are concerned. Structural changes involved in the alloy-oxide transition and hence changes of interface properties have implications for solid-electrolye gas sensing devices based on doped ceria and platinum electrodes if they are operated at high temperatures and in an atmosphere whose composition varies between a chemically oxidizing and reducing state.

Due to the high lateral resolution and the real-space imaging capabilities, we apply STM to characterize first the clean Pt(111) substrate, the growth of metallic cerium on clean Pt(111) surfaces and the subsequent formation of different incommensurate surface alloy overlayers. An intermediate surface phase with two-dimensional islands localized at Pt step edges will be described. The following sections deal with the transition of the surface alloy into CeO_2 surface phases and their geometric structures. Upon decomposition we find two-dimensional (2D) islands that we attribute to an oxidic surface phase which has not been reported yet.

II. INSTRUMENTATION AND SAMPLE PREPARATION

The experiments were carried out in an u.h.v. system equipped with a home-made beetle-type scanning tunneling microscope, a LEED/Auger four-grid optics, a preparation chamber with a Ce evaporator, and a sample transfer system. Metallic cerium (99.9%, Alfa) was evaporated from an alumina tube that was heated resistively with a tungsten wire. The microscope was operated by a RHK electronics. We used chemically etched W tips. The STM data were recorded in constant-current mode with sample bias voltages V_S ranging from -3.1 to -0.1 V. For the initial calibration the nonreconstructed $TiO_2(110)1\times1$ surface was taken where the corresponding surface lattice constant is equal to 6.49 Å.[19] A refinement of the lateral calibration was achieved by imaging the Pt(111) surface as described below. The z direction was calibrated using the height of a monoatomic step (2.26 Å).

The surface of the platinum single crystal (Pikem, U.K.) was cleaned by repeative sputtering with Ar^+ (1 kV, 1 μA, 20 min), heating in oxygen (900 K, 5×10^{-5} mbar, 15 min) which efficiently removed C impurities and annealing at 1100 K (1 h) in u.h.v.[20] This sample preparation yielded a well-ordered (as checked with LEED) and clean surface (as checked with Auger electron spectroscopy and in an independent experiment with x-ray photoemission and ion back scattering). An electron-beam source was used for heating the platinum single crystal that was clamped on a thin (1 mm) molybdenium plate. Prior to the experiments, the temperature of another sample was calibrated against the electrical power. The temperature was measured with a NiCr/Ni thermocouple that was spot-welded on top of that sample. The reproducibility of this determination was checked after the experiments.

III. EXPERIMENTAL RESULTS AND DISCUSSION

STM indicates a clean and smooth Pt(111) surface if the sample is prepared at a low base pressure and quickly transferred to the scanning tunneling microscope in the ultrahigh vacuum chamber ($p_{\mathrm{tot}}\leqslant1\times10^{-10}$ mbar). Long and narrow terraces that range in width between from less than 100 Å to several hundred Å are terminated by straight monoatomic steps. Occasionally, we also found areas with a high density of biatomic steps at the surface and phase separation between flat and stepped areas.[21] The density of monoatomic and biatomic steps varies also between different sample preparations. The step edges follow closely the high-symmetry directions of the surface, i.e., they run predominantly parallel to $\langle110\rangle$. Atomic resolved images depict a nonreconstructed (1×1) surface on terrace sites with a hexagonal arrangement of Pt surface atoms and an interatomic spacing of 2.77 Å, in agreement with the (1×1) LEED reflexes.

A. Cerium and Pt-Ce ordered surface alloys on Pt(111)

The deposition of Ce onto the Pt(111) surface at room temperature leads to spatially uniformly distributed Ce clusters without an apparent preference for an aggregation at step edges. Nominal coverages θ of Ce with respect to the Pt surface unit cell are determined with the assumption that the Ce clusters adopt the room-temperature bulk fcc structure of γ-Ce for which the lattice constant is 5.16 Å.[22] Hence the unit cell volume is equal to 137.4 Å^3 and contains four atoms. For $\theta=0.5$ ML, the clusters reveal a flat dropletlike morphology with a mean contact angle ϑ of $37\pm4°$. The quantitative evaluation yields a mean radius of 60 Å and a mean height of 15 Å where particularly the height distribution is very narrow.

A comparative study on the growth of Ce on clean Pt(111) surfaces has been previously conducted by means of low-energy electron diffraction (LEED), thermal desorption spectroscopy (TDS), Auger electron spectroscopy (AES), and STM.[16] An essentially linear dependency of the Ce and Pt Auger electron intensities versus deposition time was determined. Therefore, it was concluded that the initial growth of

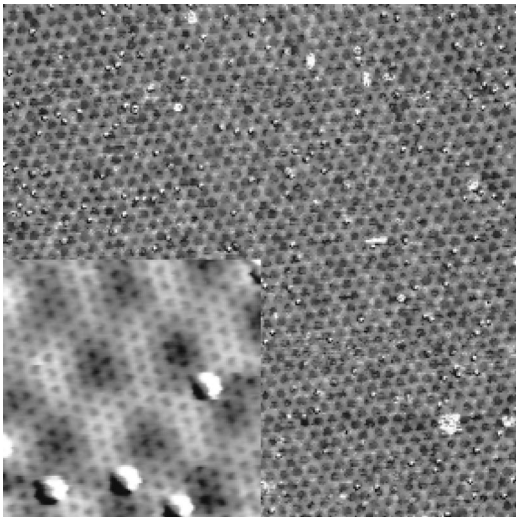

FIG. 1. STM constant-current topograph of the Pt_5Ce surface alloy ($534\times Å^2$, $V_S=-0.08$ V, $I=1.37$ nA). The nominal Ce coverage is 0.5 monolayer. Inset: Atomic resolved image (42×42 $Å^2$, $V_S=-0.08$ V, $I=0.67$ nA).

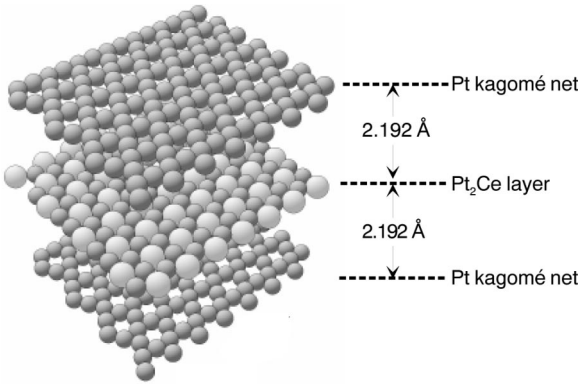

FIG. 2. Bulk crystal structure of Pt_5Ce. It consists of a hexagonal close-packed Pt layer with interatomic spacing of 2.685 Å where a quarter of lattice sites remains unoccupied thus yielding a hexagonal mesh of empty sites. It indicates a Pt_2Ce layer and so-called kagomé nets of platinum atoms. Along (0001), their positions are in registry with the Ce atoms of the Pt_2Ce layers which are separated by 5.369 Å.

Ce on Pt(111) follows the Stranski-Krastanov mode, i.e., three-dimensional clusters are formed after completion of the first monolayer. The inelastic attenuation of the Pt Auger electron intensity corresponds to a low-density layer of Ce of approximately 7.2×10^{18} atoms m^{-2} which is less than in Ce metal (8.9×10^{18} atoms m^{-2}). In an independent experiment using scanning tunneling microscopy, the authors reported that submonolayer films show close-packed Ce islands having random orientations with respect to the substrate. This is probably caused by the large lattice mismatch of 31.8% along $\langle 110\rangle$ for which the nearest-neighbor distances are 2.77 Å for Pt(111) and 3.65 Å for Ce(111).

It is not obvious from our results whether such an adlayer initially grows on the platinum surface. For the heteroepitaxial Stranski-Krastanov system Ag on Pt(111), STM studies have demonstrated that Ostwald ripening of the initially grown 2D islands occurs above 100 K.[15] It is therefore likely that Ostwald ripening of the initially formed and grown Ce nuclei has already taken place under the experimental conditions (i.e., evaporation and sample transfer at 300 K) before the sample is imaged in the tunneling microscope. Hence, conclusions on a particular growth mode at the initial stages of Ce depositions cannot be drawn from our findings.

Substantial changes of the surface morphology occur by annealing the sample ($\theta_{Ce}\approx 0.5$ ML) at 1000 K in u.h.v. This can be seen in Fig. 1 in the large-scale STM image. Two-dimensional layers are formed which can be associated with the presence of surface intermetallic compounds between Ce and Pt and which show lateral dimensions in the order of several hundred Å. The inserted image indicates the corresponding well-ordered surface alloy structure at a higher magnification from which we determine the mean interatomic spacing of 2.7 Å and the spot-spot distance of 13.7 Å in the moiré pattern. The corresponding surface unit cell of the moiré pattern is rotated by 30° with respect to surface unit cell of the alloy. Occassionally, we observed an apparent inversion of the usual contrast in our STM images (e.g., atoms are displayed as black spots as seen, for example, in the inset of Fig. 1). This effect may result from uptaking an oxygen atom by the STM tip. We also found domains with a slightly larger long-range periodicity in the moiré pattern (14.8 Å) and a different rotation of 9° with respect to the kagomé net.[25]

The Pt-Ce bulk phase diagram indicates different stiochiometric intermetallics. Previous STM, LEED, AES, and TDS studies, however, have shown the formation of a 4.4 Å high layer of Pt_5Ce if Pt(111) single crystals with submonolayer Ce overlayers are heated at 1000 K.[16] Pt_5Ce adopts the hexagonal $CaCu_5$ structure ($a=5.3685$ Å, $c=4.3830$ Å) as shown in Fig. 2.[23] The topmost surface of Pt_5Ce/Pt(111) consists of a Pt kagomé net with the closed-packed direction rotated by 30° with respect to Pt(111) (i.e., parallel to $\langle 11\bar{2}\rangle$). The presence of different domains Pt_5Ce gives rise to a $(2\times 2)+(2\times 2)R30°$ superstructure in LEED.

The moiré pattern implies an incommensurable overlayer with respect to the Pt(111) surface. For the closed-packed hexagonal surface, the coordinates of an arbitrarly chosen lattice point may be described as $[[n,m]]$ with respect to the two surface basis vectors $\mathbf{a}_1$ and $\mathbf{a}_2$. Along the vector $[n,m]$, the spacing between [[0,0]] and all lattice points lying on this vector is given by $d_i=ia\sqrt{n^2+nm+m^2}$ if a denotes the length of $|\mathbf{a}_1|=|\mathbf{a}_2|$ and i is an integer number. For symmetry reasons, one may consider only $n>m$ and $m\geqslant 0$. The angle of $[n,m]$ with respect to $a_1=[1,0]$ is then given by $\varphi_{(n,m)}=\arctan(m/2)\sqrt{3}/(n+m/2)$. Thus, one obtains $d_i=ia\sqrt{3}$ for [[1,1]] and $\varphi_{(n,m)}=30°$. Correspondingly, $d_j=jb\sqrt{s^2+st+t^2}$ holds for the vector $[s,t]$ of an incommensurable closed-packed hexagonal {111} overlayer with surface basis vectors b_1 and b_2 ($b=|b_1|=|b_2|$). They are irrationally related to a_1 and a_2. For reasons of simplicity, we describe the kagomé net as a mesh with b_1 and b_2 as basis vectors and $b=2.685$ Å. The actual unit cell forms a (2×2) superstructure with respect to this lattice. As shown in Fig. 3, large coincidence superstructure cells and nearly per-

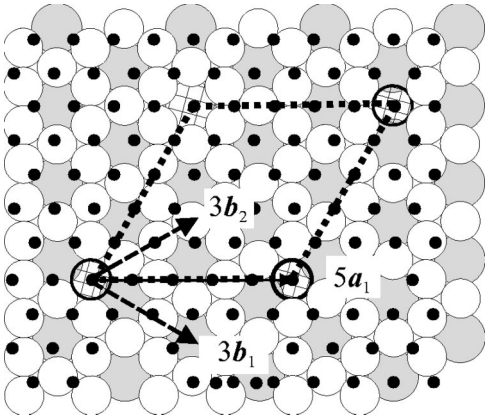

FIG. 3. Model of a domain of $Pt_5Ce(0001)$ on a Pt(111) surface (black circles). Large empty circles represent Pt atoms in the topmost kagomé layer, grey circles display the underlying Ce atoms of the Pt_2Ce layer. The Pt kagomé layer underneath is not shown. Coincidence of overlayer lattice points [[0,0]], [[3,3]], [[0,9]], and [[$\bar{3}$,6]] with lattice points [[0,0]], [[5,0]], [[0,5]], and [[5,5]] are obtained along the [0,1], [1,1], and [1,0] directions of the substrate (hatched circles). Only one coincidence superstructure cell is shown here (dotted line).

fect matching are obtained for $[s,t]=[3,3]$ (ideal spacing $d_j=jb\sqrt{27}=j\cdot 13.95$ Å, $\varphi_{(s,t)}=30°$) of the overlayer lattice and [5,0] ($d_i=ia\sqrt{25}=i\cdot 13.87$ Å, $\varphi_{(n,m)}=0°$) of the substrate lattice if one assumes an unrelaxed Pt(111) atomic arrangement at the interface and a small lattice contraction of the overlayer, i.e., by a factor of 0.994. This yields a perfect matching and $d_j=jd_{i=1}=j\cdot 13.87$ Å. In a similar fashion, registry is obtained between the overlayer lattice vectors $[s,t]=[5,1]$ (ideal spacing $d_j=jb\sqrt{31}=j\cdot 14.95$ Å, $\varphi_{(s,t)}=8.95°$, overlayer contraction by 0.982) and the substrate lattice vectors $[n,m]=[2,4]$ ($d_i=ia\sqrt{28}=i\cdot 14.68$ Å, $\varphi_{(n,m)}=40.8°$). Table I reveals the experimental STM data of the long-range periodicities $d_{j,\mathrm{STM}}$ and the angle between the mesh of moiré spots and the surface unit cell of the overlayer $\varphi_{(s,t),\mathrm{STM}}$. Within experimental errors they are in reasonable agreement with the corresponding calculated values. In addition, LEED is used to determine the rotational relationship between the overlayer and substrate lattices $\Delta\varphi_{\mathrm{LEED}}$. Both coincidence structures indicate an angle of 30° in good accordance with the calculated value of $\Delta\varphi$.

Apart from the different overlayer lattice constants, the system [5,1]‖[2,4] is consistent with bilayer structure *A* in Ref. 16 that indicates a long-range periodicity of 14.9 Å ±0.4 Å of the moiré pattern. The latter was described as a $(5.4\times 5.4)R30°$ structure with respect to the Pt(111) surface in agreement with the LEED data $[(5.6\times 5.6)R30°]$. The system [3,3]‖[5,0] corresponds to a $(4.9\times 4.9)R30°$ structure that has not yet been reported. Apparently, different sligthly rotated coincidence superstructures of Pt_5Ce coexist at the Pt(111) surface which may indicate small differences in corresponding Gibbs energies or caused by different growth rates during their formation. If one takes into account an experimental error of ±0.08 Å for the determination of interatomic spacings in our atomically resolved STM images of Pt_5Ce, the value of 2.7 Å appears to be slightly larger than the value of 2.53 Å±0.08 Å reported in Ref. 16. The spacing of 2.7 Å agrees, however, well with the ideal interatomic spacing along the closed-packed $\langle 11\bar{2}0\rangle$ directions of the Pt kagomé net (2.685 Å).

TABLE I. Measured and calculated structural data of the observed coincidence overlayer structures of Pt_5Ce/Pt(111).

$[s,t]‖[n,m]$	$d_{j,STM}$/Å [a]	$\varphi_{(s,t),\mathrm{STM}}$	d_j/Å	$\varphi_{(s,t)}$	$\Delta\varphi$ [b]
[3,3]‖[5,0]	13.7	30°	13.87	30°	30°
[5,1]‖[2,4]	14.8	9°	14.68	8.95°	31.05°

[a] $j=1$.

[b] $\Delta\varphi=\varphi_{(n,m)}-\varphi_{(s,t)}$.

It is obvious that the atomically resolved STM image does not exhibit the hexagonal superstructure of empty sites which are separated by 5.369 Å. The measured corrugation amplitudes along $\langle 110\rangle$ are 0.1 Å between the moiré spots and 0.3 Å close to the moiré spots but no larger amplitudes are found along two parallel $\langle 110\rangle$ rows that could be associated with the unoccupied atomic positions in the kagomé net. In terms of the simplified interpretation of STM images by Tersoff and Hamann, the tunneling current is proportional to the electron density at the Fermi energy E_F at the position of the tip.[24] The observed STM images could be explained with the assumption that electronic states of the underlying cerium atoms contribute to the local density of states at E_F at the empty sites.

B. 2D islands at step edges

The phase transition from a system with three-dimensional cerium clusters on platinum towards a system with two-dimensional islands of the Pt_5Ce surface alloy is thermodynamically driven and minimizes the free energy. In order to obtain intermediates of such a surface reaction, Ce overlayers have been annealed under more moderate conditions. We have chosen a temperature of 900 K which is above the melting point of 880 K of the Pt-Ce eutectics at the cerium-rich side of the phase diagram. The Pt single crystal was deposited with approximately 0.1 ML Ce. A pronounced change of the film morphology is already observed when the sample is heated at 900 K in u.h.v. for several minutes. The STM image indicates that the initially observed three-dimensional Ce clusters disappear and hexagonal 2D islands are formed that are almost symmetrically centered along step edges of the Pt(111) surface (Fig. 4). They are arranged in such a way that two opposite corners of an island are localized at the step edge with an angle between the Pt step edge and the island edges of ~120°. STM images with atomic resolution are difficult to determine due to a low corrugation (<0.05 Å) but some spots show hexagonal protrusions with interatomic spacing of 5.4 Å that corresponds to a 2×2 superstructure with respect to Pt(111) (see inset STM image in Fig. 4). However, long-range order has not developed to a large extent on these islands. The line profile along

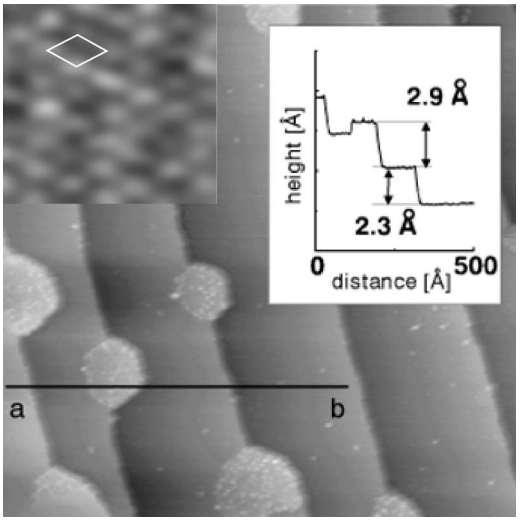

FIG. 4. STM image of the Ce/Pt(111) sample after heating at 900 K (806×806 Å^2, $V_S=-0.19$ V, $I=0.38$ nA). Inset: STM image of an island (12.8×12.8 Å^2, $V_S=-0.209$ V, $I=0.58$ nA) at higher magnification (underlined: surface unit cell with 5.4 Å $\times$5.4 Å) and line scan along a-b. Further explanations are given in the text.

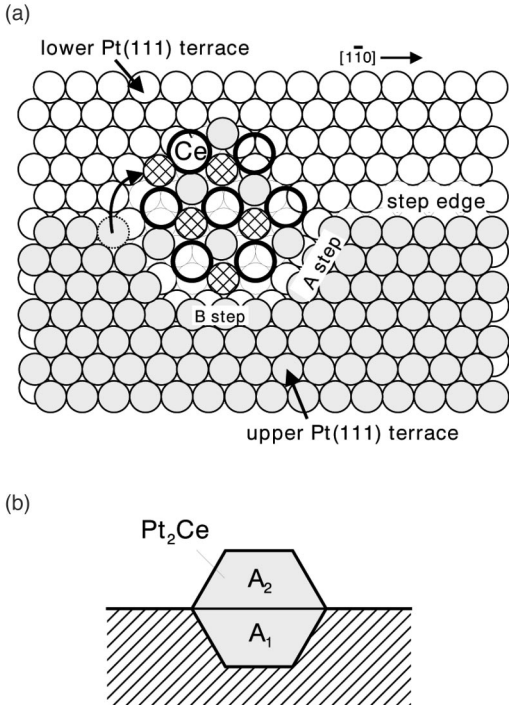

FIG. 5. (a) Schematic model of the growth mechanism of the hexagonal 2D islands. A nucleus is formed by Ce atoms (large empty circles) that are localized on fcc hollow sites of the lower Pt terrace with a local (2×2) ordered structure as well as Pt atoms from the dissolving upper terrace. These Pt atoms are localized at fcc hollow and on-top sites (hatched circles) of the lower Pt terrace. The nucleus grows over the initial step edge by incorporation of Pt atoms from the upper terrace adjacent to the boundary (arrow) as well as Ce atoms. The latter are generated during the dissolution of the Ce clusters. (b) Schematic representation of a hexagonal Pt_2Ce island along a step edge between two Pt terraces with a total area of (A_1+A_2). Further explanations are given in the text.

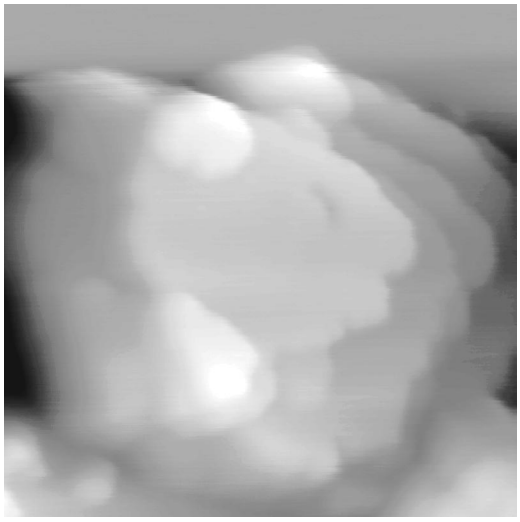

FIG. 6. STM constant-current topograph of a CeO_2 island (108×108 Å^2, $V_S=-3.1$ V, $I=0.105$ nA).

a-b is represented in the inset of Fig. 4. The apparent height of the islands is 2.9 ± 0.1 Å if the z calibration is based on the Pt single steps (2.26 Å).

A symmetric growth suggests identical rates in the directions perpendicular to the islands' edges and, particularly, identical growth rates towards and away from the Pt step edge. The formation of a Ce (2×2) adsorbate phase can be excluded since thermal energy would be sufficient to allow clustering of Ce atoms. Figure 5 serves to illustrate the proposed mechanism of the 2D island growth. It is initiated by Ce atoms nucleating at Pt step edges. At 900 K the Ce atoms reveal a sufficient high escape probability from the Ce clusters, surface mobility, and sticking probability at the step edge. A reaction takes place where platinum atoms dissolving from the step edge of the upper terrace and Ce atoms form an island with a local (2×2) structure. This island is attributed to a layer of distorted Pt_2Ce (compare Fig. 5). Its hexagonal unit cell contains one Ce atom and two Pt atoms. The latter are localized at fcc hollow and on-top sites of the underlying Pt surface. This results in out-of-plane positions of the Pt atoms with respect to the Ce plane and hence to the distortion when compared with the Pt_2Ce layer in bulk Pt_5Ce. In addition, the lattice vector of the unit cell of the distorted Pt_2Ce is slightly larger (5.548 Å instead of 5.369 Å in Pt_5Ce). The lateral density of the Pt atoms in the (111) plane of Pt (1/6.66 Å^{-2}) is twice the value of the corresponding Pt density in the Pt_2Ce layer (2/26.66 Å^{-2}). As a consequence, if the area A_1 of Pt is dissolved from the upper terrace the area $2A_1$ of Pt_2Ce is formed in accordance with the symmetric shape ($A_1=A_2$) of the islands found in STM. The hexagonal shape and the observed (2×2) ordered structure are in line with this model. Figure 5 indicates step edges which form (100) and (111) microfacets with the underlying atomic plane (so-called type A and B steps[26]) with an angle of 120° in between. The total length of A step segments is nearly twice the length of B step segments in contrast to pure monoatomically high Pt adatom islands on Pt(111). For this homoepitaxial system, B steps are energetically favored over

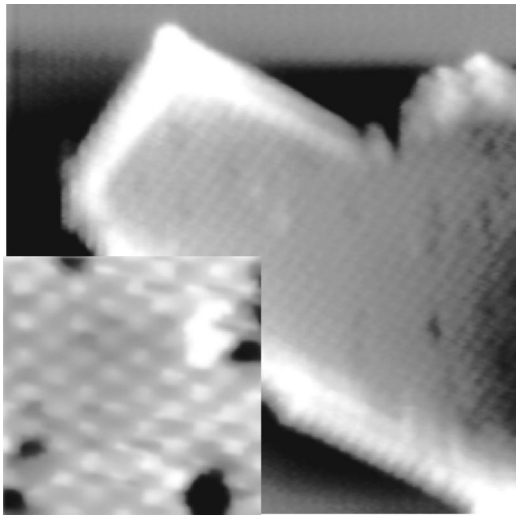

FIG. 7. STM constant-current topograph of a CeO_2 island (230×230 Å^2, $V_S=-3.1$ V, $I=0.115$ nA). The inset (29×29 Å^2, $V_S=-3.1$ V, $I=0.108$ nA) displays atomic resolution.

A steps and hence *B*-step segments are a little larger than *A*-step segments. It is very likely that the presence of Ce atoms modify the formation energies for the *A* and *B* steps or that kinetics control the actual shape of the 2D islands.

The apparent height of the 2D islands with respect to the lower Pt terrace (~2.9 Å) is slightly larger than the spacing between the on-top Pt atoms which corresponds to the diameter of Pt (2.77 Å). It is not clear yet to what extent relaxation and Ce-Pt bond formation take place or whether Ce $4f$ electronic states modify the tunneling conditions during imaging. The contribution of Ce $4f$ electronic states to the density of states at E_F would alter the measured step height with respect to the *z* calibration.

C. Cerium oxide on Pt(111)

In agreement with previous LEED studies,[11,12] the oxidation of ordered Pt_5Ce surface alloys on Pt(111) in oxygen ($p_{O_2}=5\times10^{-5}$ mbar, 1000 K) leads to pronounced changes of the morphology of the alloy islands. Photoemission data indicate that granular films are formed under these conditions which contain nonstoichiometric crystallites of a net composition of $CeO_{1.8}$ and correspondingly a significant concentration of Ce^{3+} ions in the lattice.[11] STM reveals islands with typical heights of about 20 Å and lateral dimensions in the order of 100 Å.[25] At low coverages, the majority of them is localized at step edges of the underlying Pt(111) surface (Fig. 6). Atomically flat terraces are separated by atomic steps of ~3 Å height. A complete coating of the Pt substrate can be achieved by the repeative deposition of Ce and subsequent annealing/oxidation cycles. After these treatments, oxide films are obtained which exhibit a similar granular morphology. In a recent STM study on $CeO_2(111)$ single crystal surfaces atomic resolution in STM images was obtained.[27] The observed geometric surface structure agrees well the bulk-truncated (1×1) surface of fluorite-type $CeO_2(111)$ where oxygen atoms form the outermost surface.

The fluorite-type CeO_2 lattice deserves closer attention to explain the observed step heights and atomically resolved STM images. Supposing ideal stoichiometry of CeO_2 and an idealized ionic bond model, all cerium ions exhibit an oxidation state of $+4$ and eightfold coordination. The O^{2-} ions adopt a *bcc* structure in which half of the intersticies are occupied by Ce^{4+} ions. The description is equivalent with an fcc packing of Ce^{4+} where all tetrahedral sites are occupied by O^{2-} ions thus producing a repeat of (111) planes $Ab\cdots aBc\cdots bCa\cdots cA$, etc. Here, *A*, *B*, and *C* denote different Ce positions [if one looks along (111)] and *a*, *b*, and *c* correspondingly the tetrahedreal intersticies. Interlayer distances between neighboring Ce planes (e.g., *A*-*B*) and O planes (e.g., $b\cdots a$ and *a*-*c*) are 3.124 and 1.562 Å, respectively. The points $(\cdots)$ mark the unoccupied octahedral intersticies of the fcc lattice. The interlayer distance between neighboring Ce and O planes is 0.781 Å. It follows from the geometrical relationship between the bcc and fcc representations that the eight corners of the O^{2-} cube and the Ce^{4+} at the central position correspond to particular tetrahedreal and fcc sites. These are, for example, $b_1(a_2a_3a_4)B(c_5c_6c_7)b_8$ (i.e., if one take the *aBc* stack there are always two sites of the opposite *b* layers that show the same interatomic distances than *a*-*B* and *B*-*c*). As the consequence of the electrostatic neutrality of the triple layers (i.e., *aBc* or other equivalent repeats) the (111) surface shows the highest thermodynamic stability among the low-index surfaces of CeO_2 and should be an oxygen terminated surface. The observed step height is in accordance with the spacing between equivalent (111) oxygen planes in fluorite-type CeO_2 (3.124 Å), e.g. between *a* and *b* in the layer sequence described above.

Due to the granular morphology of the CeO_2 film on Pt(111) the majority of cerium islands cannot be imaged with atomic resolution. Occasionally, smooth islands are found which are sufficiently large to obtain atomic resolved CCT's (Fig. 7). The inset image displays the (1×1) structure of $CeO_2(111)$ with a nearest-neighbor spacing of 3.9 Å. This value agrees with the ideal value of 3.826 Å along [110]. Mention should be made here of the fact that both the interatomic spacing as well as the hexagonal symmetry are in accordance with the (0001) plane of Ce_2O_3 (3.888 Å), too. This compound crystallizes in the hexagonal La_2O_3 structure. The simplified ionic model indicates the 3+ oxidation state of all cerium ions. They adopt the unusual coordination number of seven. Along [0001], Ce_2O_3 consists of hexagonal planes of oxygen and cerium ions producing an $O^{2-}_{0.5}Ce^{3+}O^{2-}O^{2-}Ce^{3+}O^{2-}_{0.5}$ repeat where $O^{2-}_{0.5}$ indicates that the corresponding oxygen planes share two unit cells. This sequence avoids a divergent surface energy. The interlayer distances are quite different if compared with the fluorite structure. They are 1.48 Å ($O^{2-}_{0.5}$-Ce^{3+}), 0.67 Å (Ce^{3+}-O^{2-}), 1.77 Å (O^{2-}-O^{2-}), 0.67 Å (O^{2-}-Ce^{3+}), and 1.48 Å (Ce^{3+}-$O^{2-}_{0.5}$). As a consequence of the charge balance, the clean oxygen-terminated $Ce_2O_3(0001)$ should indicate a (2×2) reconstruction where only half of the oxygen lattice points are occupied. Since a (2×2) superstructure is not found in LEED and STM one can exclude the formation of such Ce_2O_3 surface under the experimental conditions (p_{O_2}

$=5\times10^{-5}$ mbar, 1000 K). Previous photoemission data show $CeO_{1.8}$ which is also not consistent with Ce_2O_3. Furthermore, the observed step height ($\sim$3 Å) does not correspond to the lattice constant of Ce_2O_3 ($c=6.069$ Å).[28] The hypothetical layer sequence $O^{2-}Ce^{3+}O^{2-}$ is not stable for electrostatic reasons, in contrast to an $O^{2-}Ce^{4+}O^{2-}$ stack in CeO_2.

As we apply a negative sample bias voltage, electrons are tunneling from occupied electronic states of CeO_2 which are mainly derived from O $2p$. In addition, extended Ce $4f$ states contribute to the O $2p$ valence band[29] which indicates that the Ce-O bonds are not fully ionic but exhibit some covalency. In conclusion, the filled-state images represent oxygen ions that form the outermost surface plane. On a closer inspection of the STM images in Fig. 7, missing protrusions are found as well which may be assigned as oxygen vacancies in accordance with a previous STM study by Nörenberg *et al.*[30] They have shown that surface defects are formed on $CeO_2(111)$ single crystal surfaces during annealing of the sample at 1000 °C in ultrahigh vacuum. These defects cause a slight deviation from ideal stoichiometry CeO_{2-x}. Their self-organization was suggested to explain line defects that result during longer annealing times or higher temperatures. These line defects run in $[1\bar{1}0]$, $[0\bar{1}1]$, and $[10\bar{1}]$ directions. On contrary, the formation of such line defects cannot be established from our results on ultrathin CeO_2 layers.

D. Intermediate surface phase during CeO_2 decomposition

Our experiments indicate the complete phase transition of the ceria islands into the surface alloy within a ten minutes anneal (1000 K) of the sample. Thermodynamically stable Ce-O compounds during the decomposition of CeO_2 are Ce_nO_{2n-2} and Ce_2O_3. The stability regime of the flourite structure of CeO_2 is reached for $x>0.3$ at 1000 K (CeO_{2-x}) and the lattice cannot accommodate larger concentrations of oxygen vacancies. The transition phases Ce_nO_{2n-2} (σ phase $CeO_{1.667}$ with $n=6$, ι phase $CeO_{1.714}$ with $n=7$, ξ phase $CeO_{1.778}$ with $n=9$, ε phase $CeO_{1.800}$ $n=10$, δ phase $CeO_{1.818}$ $n=11$, and β phase $CeO_{1.833}$ with $n=12$) [31] exhibit distinct superstructures of ordered pairs of oxygen vacancies. Similar to fluorite CeO_2, these phases contain oxygen cubes (such as, e.g., $b_1(a_2a_3a_4)B(c_5c_6c_7)b_8$]. The divacancies can be explained by two unoccupied sites b_1 and b_8 at opposite corners of the oxygen cube which leads to a distorted octahedreal coordination of the central cerium ion. Further loss of oxygen yields Ce_2O_3 (i.e., $CeO_{1.5}$) in which oxygen vacancies are completely avoided in the ideal lattice. One may expect that Ce_2O_3 transforms into the alloy without formation of detectable concentrations of the thermodynamically unstable CeO.

To get more insight in the decomposition and to identify possible intermediate phases, the decomposition was carried out at lower temperatures ($\sim$900 K). Instead of the CeO_2 crystallites which disappeared completely we found patches of the Pt_5Ce surface alloy (mainly structure *A* as identified by LEED and STM) and two-dimensional islands which cannot be associated with any of the reported surface alloy

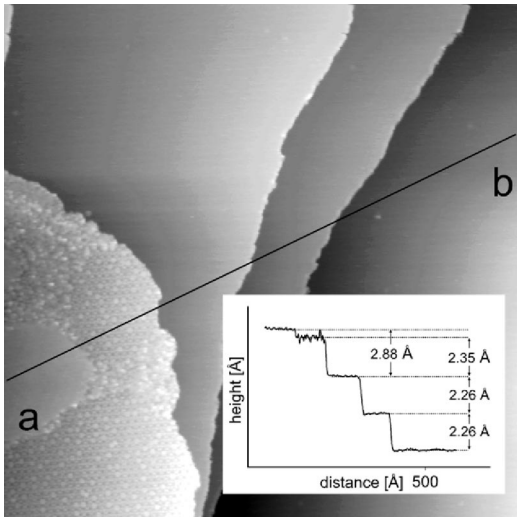

FIG. 8. STM constant-current topograph after heating the CeO_2 covered Pt(111) single crystal at 900 K and cooling to room temperature (540×540 Å^2, $V_S=-0.22$ V, $I=0.297$ nA). Inset: Line scan between *a* and *b*.

phases (Fig. 8). The STM image reveals a novel two-dimensional surface phase which is spread over the terrace of the Pt substrate. It exhibits a characteristic honeycomb structure and a height of 2.35 Å. The line scan *a*-*b* indicates also a height of $\sim$2.9 Å in the central region of the 2D island which is apparently not transformed into the honeycomb structure. This is slightly lower than the observed step height of $\sim$3 Å for CeO_2 that corresponds to a layer sequence $O^{2-}Ce^{4+}O^{2-}$. It is likely that the central regions consists of CeO_2 that forms an ultrathin layer similar to the 2D island in Fig. 9. The small reduction in thickness may indicate an $O^{2-}\cdots$Pt attraction (due to the polarization of Pt atoms) if one compares the spacing with the corresponding interlayer distance in CeO_2 ($O^{2-}Ce^{4+}O^{2-}\cdots O^{2-}$). At a few spots of

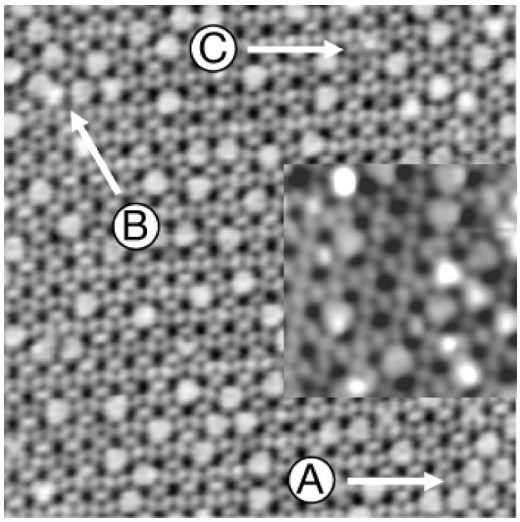

FIG. 9. STM constant-current topograph of surface-Ce_2O_3. (140×140 Å^2, $V_S=-0.22$ V, $I=0.303$ nA). Inset: Smaller scan image (44×44 Å^2) determined with $V_S=-2.99$ V, $I=0.05$ nA. Further explanations are given in the text.

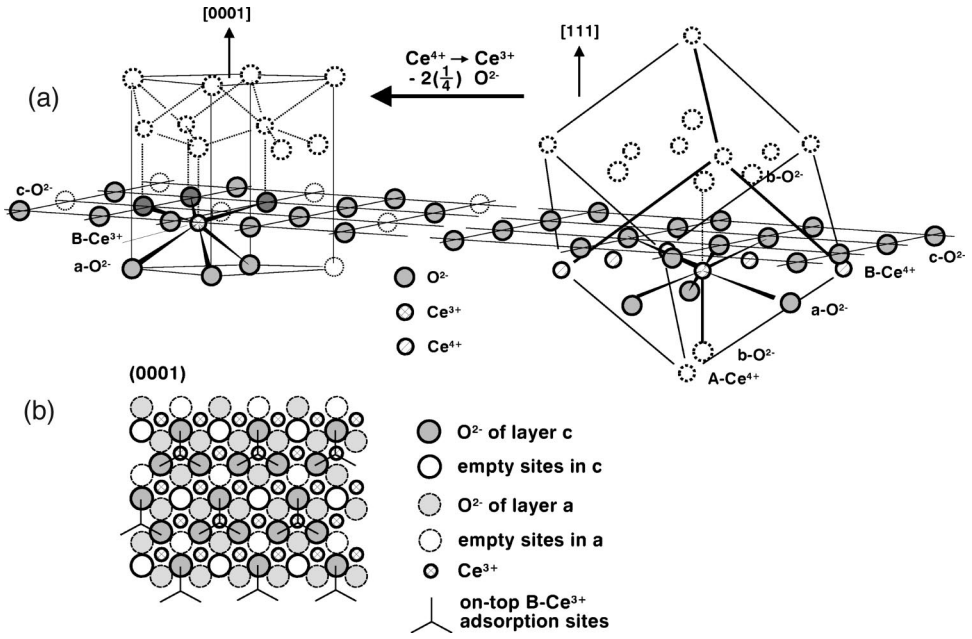

FIG. 10. (a) Schematic model of the transformation of an $O^{2-}Ce^{4+}O^{2-}$ layer sequence into $O^{2-}_{3/4}Ce^{3+}O^{2-}_{3/4}$ and the crystallographic relationships with the bulk unit cells of Ce_2O_3 (left-hand side) and CeO_2 (right-hand side), respectively. (b) Top-view of surface-Ce_2O_3 with the surface normal parallel to the [111] orientation of Pt(111). For clarification, ions are drawn smaller than their actual sizes.

the honeycomb structure a high concentration of adsorbed atoms is found that extend from the nontransformed parts to the boundary zone close to the platinum. On contrary, such adatoms are not visible at the surface of the nontransformed parts nor at the Pt surface.

Figure 9 shows the honeycomb structure at a higher magnification. We find that the surface can be imaged by applying negative sample voltages over a wide range (compare the inset in Fig. 9) without obvious differences in the observed surface structures. The hexagonal arrangement with an occupancy of 3/4 of surface sites looks similar to the platinum kagomé nets in Pt_5Ce, however, the spacing between the black holes is 7.8 Å instead of 5.369 Å in the alloy. The nearest neighbor distance along closely packed rows is 3.9 Å which agrees with the lattice constants of $Ce_2O_3(0001)$ (3.888 Å) as well as $CeO_2(111)$ (3.826 Å). The lattice constant of the observed hexagonal surface unit cell is approximately twice the lattice constants of nonreconstructed $Ce_2O_3(0001)$ and $CeO_2(111)$ but the unit cell contains one atom less than the corresponding 2×2 cells of these surfaces. The transition phases Ce_nO_{2n-2} are excluded since none of these phases shows such dense superstructures of oxygen vacancies. So far, such an ultrathin and epitaxial two-dimensional surface phase has not yet been reported for the system $CeO_2/Pt(111)$ to our knowledge. The observed thickness is a little smaller than half the lattice constant $c = 6.069$ Å in Ce_2O_3.

Consideration of charge balance indicates that electrostatic neutrality of $O^{2-}Ce^{3+}O^{2-}$ is achieved if a quarter of O^{2-} ions is being removed in each oxygen layer thus forming layers of a composition $(O_{3/4}\square_{1/4})$. Here $\square$ denotes the empty sites. A regular arrangement of a quarter of missing protrusions is exactly what is seen in the STM image. This phase may be termed as surface-Ce_2O_3. Figure 10(a) demonstrates schematically the transformation of an $O^{2-}Ce^{4+}O^{2-}$ layer sequence into $O^{2-}_{3/4}Ce^{3+}O^{2-}_{3/4}$ and the crystallographic relationships of these stacks with the bulk unit cells of Ce_2O_3 (left-hand side) and CeO_2 (right-hand side). Here, a and c denote the $(O_{3/4}\square_{1/4})$ layers of $O^{2-}_{3/4}Ce^{3+}O^{2-}_{3/4}$ with a Ce^{3+} layer in-between. A corresponding sequence of layers in $O^{2-}Ce^{4+}O^{2-}$ is, for example, aBc. The transformation involves reduction of Ce^{4+} to Ce^{3+} and desorption of oxygen, thus creating unoccupied lattice sites in the oxygen planes. The bulk unit cell of Ce_2O_3 reveals an asymmetric spacing between Ce^{3+} and the neighboring oxygen planes (B-c0.67 Å and a-B1.48 Å), simply speaking as the result of the Coulombic attraction of the negatively charged $O^{2-}Ce^{3+}O^{2-}$ stack above (dotted circles in the left-hand scheme in Fig. 10). A corresponding electrostatic force is not built up in $O^{2-}_{3/4}Ce^{3+}O^{2-}_{3/4}$ which presumably leads to atomic displacements with respect to the ideal lattice positions. This results in a relaxed surface-Ce_2O_3 phase as indicated in Fig. 10(b) (top-view).

Surprisingly, filled-state images of the surface-Ce_2O_3 phase can be obtained at low negative sample voltages (e.g., 0.22 V, compare Figs. 8 and 9). A previous study with high-resolution electron loss and ultraviolet photoemission spectroscopy has shown an empty ($^1S_0$, binding energy 0.7 eV with respect to the Fermi energy) and a filled Ce $4f$ state (spin-orbit split $^2F_{7/2}$ and $^2F_{5/2}$, at -1.5 eV) in stoichiometric CeO_2 and nonstoichiometric (i.e., Ce^{3+}-containing) cerium oxide films, respectively.[18] The Ce $4f$ state is strongly localized and contains an O $2p$ contribution.[32] Valence band photoemission spectra of ultrathin CeO_2 layers on Pt(111) indicate a width-at-half maximum of $\sim$1.1 eV of the Ce $4f$ state (taken at a photon energy of 120 eV and with a resolution of 100 meV).[17] The photoemission intensity is very low at -0.2 eV. Presumeably, the high work function of the underlying platinum causes band bending or charging effects due to electron transfer which decreases the binding energies of the electronic states. Obviously, the density of states is then sufficient to image surface-Ce_2O_3. One would also anticipate different STM images at sample voltages of

~ -3 V (i.e., tunneling into valence band states) and ~ -0.2 V. This is apparently not observed probably due to a strong Ce $4f$-O $2p$ intermixing in surface-Ce_2O_3.

Figure 10(b) shows that the surface provides two kinds of threefold hollow adsorption sites which exhibit the symmetry properties of the point group C_{3v}. One is located on top of a B-Ce^{3+} while the others lie over empty sites, c-□. Both adsorption sites form 1×1 superstructures with respect to the unit cell of surface-Ce_2O_3. By comparison with the bulk unit cell of Ce_2O_3 it is obvious that the adsorption of oxygen at B-Ce^{3+} sites leads to a sevenfold coordination of the central Ce^{3+} ion which is quite similar to bulk Ce_2O_3 [compare Fig. 10(a)]. The second type of on-top adsorption sites is formed by two O^{2-} ions and one □ site and hence reveals a lower symmetry.

It is noteworthy to inspect the bright spots in the STM image in more detail which we attribute to adsorbed atoms or molecules. The overwhelming majority of the adsorbates are localized at hollow sites formed by three atoms. In terms of the proposed structure model they are associated with B-Ce^{3+} sites. On a few spots of the surface, the beginning formation of a commensurate layer of adsorbates with a local 1×1 superstructure is recognizable (compare arrow A in Fig. 9). In contrast, the adsorption at two adjacent hollow sites is almost negligible (arrow B) so that occupation of the second type of B-Ce^{3+} sites (which is formed by two O^{2-} and one empty site) can be neglected. Apparently, the adsorption onto the missing protrusions (i.e., sites c-□) is extremely rarely (arrow C). This may be explained by the proposed structure of the islands where the unoccupied sites cannot be considered as crystallographic lattice points. Particularly, they do not react like randomly distributed oxygen vacancies V_O^{2+} that are formed usually on oxide surfaces by thermal desorption of molecular oxygen ($2\ O^{2-}_{\text{lattice}} \rightarrow O_2 + V_O^{2+} + 2e^-$). This type of point defect was shown to readily adsorb molecules such as O_2 or CO that are exposed, for example, to the surfaces of ZnO and TiO_2.[33] One may conclude from the 3D and 2D morphologies of CeO_2 crystallites and surface-Ce_2O_3 that the $CeO_2 \rightarrow$surface$-Ce_2O_3$ transformation involves the diffusion of cerium and oxygen over the surface-Ce_2O_3 phase and the growth at the boundary of the islands. This assumption explains the observed inhomogeneous distribution of adatoms in the STM image in Fig. 8. It is, however, not possible to achieve a chemical contrast through different sample voltages in our STM experiments and to address the question of the chemical nature of the observed adatoms.

IV. CONCLUSIONS

The surface alloying of metallic cerium deposits with Pt(111) 1×1 single crystal surfaces occurs at 1000 K and leads to well ordered two-dimensional overlayers. Atomically resolved STM images and the observed moiré superstructures are consistent with the formation of an incommensurate adlayer of Pt_5Ce where the uppermost atomic layer consists of a Pt kagomé net. We find a large-coincidence overlayer structure with a spacing of 13.7 Å. If the annealing is performed at 900 K, two-dimensional islands of hexagonal shape are formed at the step edges of the Pt surface. A 2×2 superstructure with respect to Pt(111) is identified. It is likely that the incommensurate Pt_5Ce surface alloy islands are formed from such commensurate 2D islands which hence could act as intermediate phase in surface alloying between Pt and Ce.

The oxidation with O_2 at $T=1000$ K transforms the Pt_5Ce islands into defective CeO_2 crystallites that are composed of several atomic layers. The step heights correspond to the interlayer distance between two equivalent (111) planes in fluorite-type CeO_2. Atomic resolved STM images are obtained only for islands with a height of a ''monolayer'' which contains a layer sequence $O^{2-}Ce^{4+}O^{2-}$. They indicate the hexagonal lattice of O^{2-} ions and missing protrusions that are attributed to oxygen vacancies.

The oxide $\rightarrow$ alloy phase transition takes place at 1000 K. Upon heating at a lower temperature of 900 K, we observed a surface structure by STM which is assigned to an ordered layer of surface-Ce_2O_3. This phase, however, does not exhibit the corresponding bulk structure of Ce_2O_3. STM shows a honeycomb arrangement of missing protrusions and an inhomogeneous distribution of adatoms.

*Electronic address: schierb@uni-duesseldorf.de

[1] V. Maurice, S. Cadot, and P. Maurice, Surf. Sci. **471**, 33 (2001).
[2] M. Bäumer, M. Frank, R. Kühnemuth, S. Stempel, and H. Freund, Surf. Sci. **454-456**, 957 (2000).
[3] H. Freund, Faraday Discuss. **114**, 1 (1999).
[4] S. Shaikhutdinov, M. Ritter, X. Wang, H. Over, and W. Weiss, Phys. Rev. B **60**, 11 062 (1999).
[5] K. Lewis, S. Oyama, and G. Somorjai, Surf. Sci. **233**, 75 (1990).
[6] S. Surnev, L. Vitali, M. Ramsey, F. Netzer, G. Kresse, and J. Hafner, Phys. Rev. B **61**, 13 945 (2000).
[7] D. Mullins, P. Radulovic, and S. Overbury, Surf. Sci. **429**, 186 (1999).
[8] N. Condon, F. Leibsle, A. Lennie, P. Murray, D. Vaughan, and G. Thornton, Phys. Rev. Lett. **75**, 1961 (1995).
[9] X. Wang, W. Weiss, S. Shaikhutdinov, M. Ritter, M. Petersen, F. Wagner, R. Schloegl, and M. Scheffler, Phys. Rev. Lett. **81**, 1038 (1998).
[10] S. Surnev, G. Kresse, M. Ramsey, and F. Netzer, Phys. Rev. Lett. **87**, 086 102 (2001).
[11] K. Schierbaum, Surf. Sci. **399**, 29 (1998).
[12] C. Hardacre, G. Roe, and R. Lambert, Surf. Sci. **326**, 1 (1995).
[13] F. Besenbacher, L. Nielsen, D. A. King, and D. Woodruff, Vol. 8 of *the Physics of Solid Surfaces*, in *Growth and Properties of Ultrathin Epitaxial Layers* (Elsevier, Amsterdam, 1997).
[14] L. Zhang, J. van Ek, and U. Diebold, Phys. Rev. B **57**, R4285 (1998).
[15] H. Brune, H. Röder, C. Boragno, and K. Kern, Phys. Rev. B **49**, 2997 (1994).
[16] C. Baddeley, A. Stephenson, C. Hardacre, M. Tikhov, and R. Lambert, Phys. Rev. B **56**, 12 589 (1997).
[17] U. Berner, K. Schierbaum, G. Jones, P. Wincott, S. Haq, and G. Thornton, Surf. Sci. **467**, 201 (2000).

[18] A. Pfau and K. Schierbaum, Surf. Sci. **321**, 71 (1994).
[19] V. Henrich and P. Cox, *The Surface Science of Metal Oxides* (Cambridge University Press, Cambridge, 1994).
[20] A. Ramstad, F. Strisland, S. Raaen, T. Worren, A. Borg, and C. Berg, Surf. Sci. **425**, 57 (1999).
[21] P. Grütter and U. Düring, Phys. Rev. B **49**, 2021 (1994).
[22] B. Predel, *Landolt-Börnstein, Numerical Data and Functional Relationships in Science and Technology, New Series IV/5a* (Springer-Verlag, Heidelberg, 1993).
[23] B. Predel, *Landolt-Börnstein, Numerical Data and Functional Relationships in Science and Technology, New Series IV/5c* (Springer-Verlag, Heidelberg, 1993).
[24] J. Wintterlin, H. J. Guntherodt, and R. Wiesendanger, in *Scanning Tunneling Microscopy I* (Springer-Verlag, Berlin, Heidelberg, 1994).
[25] U. Berner and K. D. Schierbaum, Thin Solid Films **400**, 46 (2001).
[26] T. Michely, M. Hohage, M. Bott, and G. Comsa, Phys. Rev. Lett. **70**, 3943 (1993).
[27] H. Nörenberg and G. Briggs, Surf. Sci. **402-404**, 734 (1998).
[28] R. Wyckoff, *Crystal Structures* (Interscience New York, 1964), Vol. 2.
[29] D. D. Koelling, A. M. Boring, and J. H. Wood, Solid State Commun. **47**, 227 (1983).
[30] H. Nörenberg and G. Briggs, Surf. Sci. **424**, L352 (1999).
[31] P. Kunzmann and L. Eyring, J. Solid State Chem. **14**, 229 (1975).
[32] W.-D. Schneider, B. Delley, E. Wuilloud, J.-M. Ilmer, and Y. Baer, Phys. Rev. B **32**, 6819 (1985).
[33] W. Göpel, J. A. Anderson, D. Frankel, M. Jaehning, K. Phillips, J. A. Schäfer, and G. Rocker, Surf. Sci. **139**, 333 (1984).